

Two-dimensional simulation of fast gas heating in an atmospheric pressure streamer discharge and humidity effects

This content has been downloaded from IOPscience. Please scroll down to see the full text.

2014 J. Phys. D: Appl. Phys. 47 155202

(<http://iopscience.iop.org/0022-3727/47/15/155202>)

View [the table of contents for this issue](#), or go to the [journal homepage](#) for more

Download details:

IP Address: 93.180.48.67

This content was downloaded on 20/09/2016 at 14:02

Please note that [terms and conditions apply](#).

You may also be interested in:

[Numerical simulation for production of O and N radicals in an atmospheric-pressure streamer discharge](#)

Atsushi Komuro, Ryo Ono and Tetsuji Oda

[Vibration-to-translation energy transfer in atmospheric-pressure streamer discharge in dry and humid air](#)

Atsushi Komuro, Kazunori Takahashi and Akira Ando

[Behaviour of OH radicals in an atmospheric-pressure streamer discharge studied by two-dimensional numerical simulation](#)

Atsushi Komuro, Ryo Ono and Tetsuji Oda

[Effects of pulse voltage rise rate on velocity, diameter and radical production of an atmospheric-pressure streamer discharge](#)

Atsushi Komuro, Ryo Ono and Tetsuji Oda

[Numerical simulation for the production of chemically active species in primary and secondary streamers in atmospheric-pressure dry air](#)

Atsushi Komuro, Kazunori Takahashi and Akira Ando

Two-dimensional simulation of fast gas heating in an atmospheric pressure streamer discharge and humidity effects

Atsushi Komuro and Ryo Ono

Department of Advanced Energy, The University of Tokyo, 5-1-5 Kashiwanoha, Kashiwa, Chiba, 227-8568, Japan

E-mail: komuro@streamer.t.u-tokyo.ac.jp and ryo-ono@k.u-tokyo.ac.jp

Received 25 November 2013, revised 2 February 2014

Accepted for publication 6 February 2014

Published 27 March 2014

Abstract

Gas heating in an atmospheric-pressure streamer discharge was analysed by a two-dimensional streamer discharge simulation model describing internal molecular energy transfer. Our two-dimensional streamer simulation model incorporates concepts from the fast gas heating mechanism proposed by Popov (2011 *J. Phys. D: Appl. Phys.* **44** 285201) and our self-developed state-to-state vibrational kinetics. In dry air, gas heating occurs mainly from electron-impact dissociation reactions of O₂ molecules and from quenching processes of electronically excited N₂(*B* ³Π_g, *C* ³Π_u) molecules and O(¹D) atoms. In humid air, rapid vibration-to-translation transitions of H₂O and the exothermicity of the OH formation reactions additionally increase the gas temperature. It is shown that gas heating during the discharge pulse increases with humidity.

Keywords: streamer discharge, numerical simulation, radical production, gas heating, chemical reaction

(Some figures may appear in colour only in the online journal)

1. Introduction

Atmospheric pressure plasmas have great potential for many applications as efficient sources of active species (e.g. radicals, charged particles, excited species, and UV radiation) [2–7]. Medical applications of plasmas have especially attracted great interest recently [8, 9]. Researchers in disparate fields, such as engineers and medical scientists, work together to develop plasma medicine for new cancer therapies or wound treatment methods. Presently, experimental studies of plasmas always precede theoretical studies that support experimental results. Therefore, current technical development of atmospheric pressure plasmas depends not on theory, but rather on empirical knowledge. In order to demonstrate the validity and safety of plasma technologies, simulation models that can correctly reproduce the phenomena must be developed as soon as possible.

Gas heating in atmospheric pressure plasmas is one of the important characteristics that determine the efficiency of

plasma applications. Though atmospheric pressure plasmas are generally thought of as low temperature plasmas [10, 11], experimental results show that the gas temperature in a pulsed positive streamer discharge under atmospheric-pressure air can increase by more than 100 K near the point anode during the early post-discharge period [12, 13]. This temperature rise affects chemical reaction rates occurring in the post-discharge phase [14], and additionally introduces instability in the discharge, which can lead to spark formation [15–17]. The gas-heating effect is not negligible for plasma applications.

The energy supplied to a discharge space by an applied voltage pulse is partially stored as internal energy in background gas molecules. Then, this stored energy is gradually dissipated as the molecules relax toward the thermal equilibrium state. Figure 1 depicts the time variation of energy transferred from the discharge pulse to various molecular energy modes. In an atmospheric pressure plasma, a large amount of the discharge energy is stored in vibrational modes, and the rest of the energy goes to

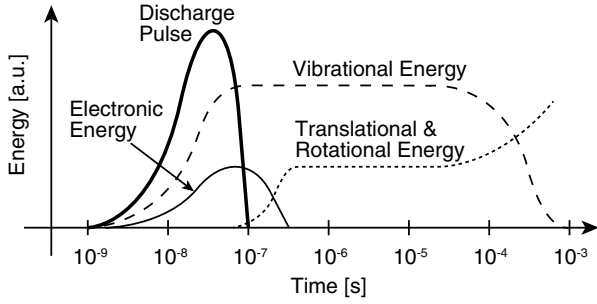


Figure 1. Conceptual diagram of the discharge energy transfer to background gas molecules.

the electronic, rotational, and translational modes [14, 18]. Rotational and translational energies are assumed to instantly reach equilibrium because the translational-to-translational and rotational-to-translational relaxation time constants are shorter than the general discharge pulse at atmospheric pressure [10, 19]. Electronic energy is mainly released through quenching reactions, whose time constants are faster than $1 \mu\text{s}$ under atmospheric pressure at room temperature [20, 21]. After the electronic energy relaxes to the thermal equilibrium state, vibrational energy relaxation begins. According to the nature of the gas involved in the discharge, different models are required to evaluate the energy transfer rates.

Energy relaxation from different energy modes temporarily increases the gas temperature [14] as shown in figure 1. The second increase in the gas temperature is well understood as an effect of vibrational energy relaxation [14, 23, 24]. On the other hand, the first increase, which occurs during the discharge pulse, is presently under investigation. Marode *et al* proposed for the first time the question for the fast gas heating in a streamer channel [16]. Then, the gas temperature in the streamer channel experimentally estimated by the measurements of the second positive system of N_2 emission [22]. In [22], a temperature of 400 K has been measured within the secondary streamer in this early period. Popov [25, 1] showed in his axis-symmetric one-dimensional simulation model that fast gas heating during the discharge pulse is caused by the enthalpy of the dissociation reactions of N_2 and O_2 , the quenching reaction of electronically excited N_2 molecules by O_2 , and the quenching reaction of $\text{O}(^1\text{D})$ by N_2 . Marode *et al* used the Popov's fast heating approach in his one-dimensional simulation for studying the secondary streamer [28]. Aleksandrov *et al* [17] also developed a fast gas heating model by comparing with their experimental results. Tholin and Bourdon [26] performed two-dimensional simulations for a nanosecond spark discharge with a reduced chemical reaction model using the η_R value, which is the fraction of discharge energy converted to gas heating, calculated by Popov [1] and Aleksandrov *et al* [17].

The effects of humidity on the fast gas heating have also been investigated in this paper. Gas heating resulting from ion-molecule reactions involving H_2O was studied in [1] and showed that humidity played no role in gas heating. However, our experimental results showed that the rotational temperatures of OH and NO just after the discharge, at times much faster than vibrational relaxation, in humid air are over

100 K higher than that in dry air [12, 13]. These experimental data need to be validated theoretically.

In this paper, the mechanism of a fast gas heating is analysed using our axis-symmetric two-dimensional simulation model [27] and the effects of gas heating on the discharge kinetics in a pulsed positive streamer discharge under atmospheric-pressure air are investigated. In addition, the effect of humidity on the fast gas heating system is analysed through comparison with our previous experimental results.

2. Simulation model

2.1. Model of discharge

To compute the streamer propagation in air, we use the first-order electrohydrodynamic model for electrons and positive and negative ions in the framework of the drift-diffusion approximation [30–32]. Thus, the equations involved in this model are as follows:

$$\frac{\partial n_s}{\partial t} + \text{div}(n_s \mathbf{v}_s(E/N)) = S_s(E/N), \quad s = e, p, n, \quad (1)$$

$$n_e \mathbf{v}_e(E/N) = n_e \mu_e(E/N) \mathbf{E} - D_e(E/N) \text{grad}(n_e), \quad (2)$$

$$n_p \mathbf{v}_p(E/N) = n_p \mu_p(E/N) \mathbf{E}, \quad (3)$$

$$n_n \mathbf{v}_n(E/N) = n_n \mu_n(E/N) \mathbf{E}, \quad (4)$$

$$\text{div} \mathbf{E} = \frac{e}{\epsilon_0} (n_p - n_e - n_n), \quad (5)$$

where n_s , $\mathbf{v}_s(E/N)$, $S_s(E/N)$, $\mu_s(E/N)$, and $D_s(E/N)$ are the charged particle density, charged particle velocity, particle chemical source term, mobility, and diffusion coefficient, respectively. The subscript 's' denotes electrons (e) or positive (p) or negative (n) ions. \mathbf{E} is the electric field, ϵ_0 is the permittivity of free space, and e is the absolute value of the electronic charge. The electron transport and source parameters (such as \mathbf{v}_e , D_e , and the reaction coefficients in S_s) are calculated using Bolsig+ [33] with published e–V cross sections [34–36]. We used a reduced reaction model including electron-impact collisions (excitation, ionization, dissociation, recombination, attachment, and detachment), ion recombination, and reactions of neutrals. In the chemical reaction model, excited N_2 and O_2 molecules correspond to effective states clustered around actual molecular levels as described in table 1, in accordance with the method proposed by Fresnet *et al* [37]. The reactions involving electron-impact collisions considered in the model are listed in table 2 and other reactions are shown in our previous paper [27]. In (3) and (4), all ion mobilities are assumed to be $2.2 \times 10^{-4} \text{ m}^2 \text{ V}^{-1} \text{ s}^{-1}$ [38] and diffusion is neglected for the ionic species. The initial gas temperature is set to 300 K for the whole area. Photoionization is described by the three-exponential Helmholtz models [39, 40]. The charged species transport equation (1) is solved using the MUSCL superbee algorithm [41]. The electrical potential (5) is calculated by separately considering the Poisson and Laplace fields. An analytical solution is used for the Laplace field calculation [42]. To solve Poisson's equation, we use the red-black multigrid

Table 1. Effective electronic states of N₂ and O₂ considered in this simulation.

Electronic state	Excitation energy (eV)	Effective state
N ₂ (X, v = 0)	0	N ₂ (X)
N ₂ (A ³ Σ _u ⁺ , v = 0–4)	6.17	N ₂ (A ₁)
N ₂ (A ³ Σ _u ⁺ , v = 5–9)	7.00	N ₂ (A ₂)
N ₂ (B ³ Π _g)	7.35	N ₂ (B)
₂ (W ³ Δ _u)	7.36	N ₂ (B)
N ₂ (A ³ Σ _u ⁺ , v > 10)	7.80	N ₂ (B)
N ₂ (B' ³ Σ _u ⁻)	8.16	N ₂ (B)
N ₂ (a' ¹ Σ _u ⁻)	8.40	N ₂ (a)
N ₂ (a ¹ Π _g)	8.55	N ₂ (a)
N ₂ (w ¹ Δ _u)	8.89	N ₂ (a)
N ₂ (C ³ Π _u)	11.03	N ₂ (C)
N ₂ (E ³ Σ _g ⁺)	11.88	N ₂ (E)
N ₂ (a'' ¹ Σ _g ⁺)	12.25	N ₂ (E)
O ₂ (a ¹ Δ _g)	0.977	O ₂ (a)
O ₂ (b ¹ Σ _g ⁺)	1.627	O ₂ (b)

method [43] and perform the calculation on a graphics processing unit (GPU) [44]. Using this powerful computing method, the time required to solve Poisson's equation is 40 times less than that when the calculations are performed with a single-core CPU. However, it still needs improvement because the computation time for overall simulation is about 240 h by using a general-purpose PC. Detailed numerical techniques, including methods for solving (1) and (5), are given in our previous paper [45].

Figure 2 shows the computation domain. To simulate the streamer discharge, we chose a cylindrical domain of 18 mm height and 8 mm radius. The total number of grid points is $N_z \times N_r = 1792 \times 256$ with spatial steps from $\delta z = 1 \mu\text{m}$ (near the point anode and plane cathode) to $10 \mu\text{m}$ (at the interelectrode gap) [46] in the z -direction and from $\delta r = 2.5 \mu\text{m}$ to $200 \mu\text{m}$ in the r -direction. The point electrode takes the form of a hyperboloid of revolution with a radius of $40 \mu\text{m}$, corresponding to that used in our previous experimental setup. At the conducting anode, the positive ion fluxes are fixed to zero, while the negative ion and electron fluxes are estimated using the Neumann boundary condition [30]. At the conducting cathode, the Neumann boundary condition is applied to all positively and negatively charged fluxes [30]. The experimentally obtained shape of the voltage pulse in figure 3 is input at the point electrode domain. Figure 4 shows an example of the simulation results. Figures 4(a) and (b) show two-dimensional distributions of streamer light emitted at (a) $t = 10 \text{ ns}$ (primary streamer) and (b) $t = 50 \text{ ns}$ (secondary streamer). The methods used to simulate the emissions are explained in [45]. Figure 4(c) shows the axial distributions of the reduced electric field, E/N , corresponding to figures 4(a) and (b). The E/N at the primary streamer head is approximately 800 Td ($1 \text{ Td} = 10^{-17} \text{ V cm}^2$), and that of the secondary streamer is approximately 110–120 Td. Further details of the simulation model are given in [27, 45].

2.2. Model of gas heating

In this paper, energy stored in translational and rotational modes is assumed to instantly reach equilibrium because

Table 2. Considered reactions involving electron-impact collisions.

Reaction	Threshold energy (eV)
(1) N ₂ + e ⁻ → N ₂ (Elastic) + e ⁻	$f(E/N)$
(2) N ₂ + e ⁻ → N ₂ (Rot) + e ⁻	0.02
(3) N ₂ + e ⁻ → N ₂ (v = 1) + e ⁻	0.29
(4) N ₂ + e ⁻ → N ₂ (v = 2) + e ⁻	0.59
(5) N ₂ + e ⁻ → N ₂ (v = 3) + e ⁻	0.88
(6) N ₂ + e ⁻ → N ₂ (v = 4) + e ⁻	1.17
(7) N ₂ + e ⁻ → N ₂ (v = 5) + e ⁻	1.47
(8) N ₂ + e ⁻ → N ₂ (v = 6) + e ⁻	1.76
(9) N ₂ + e ⁻ → N ₂ (v = 7) + e ⁻	2.06
(10) N ₂ + e ⁻ → N ₂ (v = 8) + e ⁻	2.35
(11) N ₂ + e ⁻ → N ₂ (A ₁) + e ⁻	6.17
(12) N ₂ + e ⁻ → N ₂ (A ₂) + e ⁻	7.00
(13) N ₂ + e ⁻ → N ₂ (B) + e ⁻	7.35
(14) N ₂ + e ⁻ → N ₂ (a) + e ⁻	8.40
(15) N ₂ + e ⁻ → N ₂ (C) + e ⁻	11.03
(16) N ₂ + e ⁻ → N ₂ (E) + e ⁻	11.88
(17) N ₂ + e ⁻ → N(⁴ S) + N(² D) + e ⁻	13.00
(18) N ₂ + e ⁻ → N ₂ ⁺ + 2e ⁻	15.60
(19) N ₂ + e ⁻ → N ₂ ⁺ (B ² Σ _u ⁺) + e ⁻	18.80
(20) O ₂ + e ⁻ → O ₂ (Elastic) + e ⁻	$f(E/N)$
(21) O ₂ + e ⁻ → O ₂ (Rot) + e ⁻	0.02
(22) O ₂ + e ⁻ → O ₂ (v = 1) + e ⁻	0.19
(23) O ₂ + e ⁻ → O ₂ (v = 2) + e ⁻	0.38
(24) O ₂ + e ⁻ → O ₂ (v = 3) + e ⁻	0.57
(25) O ₂ + e ⁻ → O ₂ (v = 4) + e ⁻	0.75
(26) O ₂ + e ⁻ → O ₂ (a) + e ⁻	0.98
(27) O ₂ + e ⁻ → O ₂ (b) + e ⁻	1.63
(28) O ₂ + e ⁻ → O(³ P) + O(³ P) + e ⁻	6.00
(29) O ₂ + e ⁻ → O(¹ D) + O(³ P) + e ⁻	8.40
(30) O ₂ + e ⁻ → O(¹ S) + O(³ P) + e ⁻	9.97
(31) O ₂ + e ⁻ → O ₂ ⁺ + 2e ⁻	12.06
(32) O ₂ + e ⁻ → O ₂ ⁻ (² P) + O(³ P)	$f(E/N)$
(33) O ₂ + O ₂ + e ⁻ → O ₂ ⁻ + O ₂	$f(E/N)$
(34) H ₂ O + e ⁻ → H ₂ O(Elastic) + e ⁻	$f(E/N)$
(35) H ₂ O + e ⁻ → H ₂ O(v ₂ = 1) + e ⁻	0.20
(36) H ₂ O + e ⁻ → H ₂ O(v ₁ = 1) + e ⁻	0.43
(37) H ₂ O + e ⁻ → H ₂ O(v ₃ = 1) + e ⁻	0.43
(38) H ₂ O + e ⁻ → H + OH + e ⁻	7.00
(39) H ₂ O + e ⁻ → O(P) + H ₂ + e ⁻	13.00
(40) H ₂ O + e ⁻ → H ₂ O ⁺ + 2e ⁻	13.00
(41) H ₂ O + e ⁻ → OH ⁻ + H	3.58
(42) H ₂ O + e ⁻ → H ⁻ + OH	4.36
(43) H ₂ O + e ⁻ → H ₂ + O ⁻	3.28

translational-to-translational relaxation occurs within a few collisions between the heavy species and rotational-to-translational relaxation takes place within a few dozen molecular collisions [10]. Therefore, heat released from these relaxation processes is equally distributed to the translational and rotational modes. Figure 5 shows that the energy loss fraction depends on E/N . The energy loss fraction for a reaction, for example, $M + e^- \rightarrow M^* + e^-$, is calculated by $\epsilon \times [M] \times f(E/N)$, where ϵ is the reaction threshold energy, $[M]$ is the number density of molecule M , and $f(E/N)$ is the reaction rate. The reaction rates are calculated by Bolsig+. The discharge energy may be used to predominately produce N(²D), N(⁴S), and N₂⁺ at the primary streamer head, because E/N at the primary streamer head is approximately 800 Td. In the secondary streamer, the discharge energy may be used to produce N₂(v), O(¹D), O(³P), and N₂(C ³Π_u). Following the relaxation processes of these excited molecules allows insight

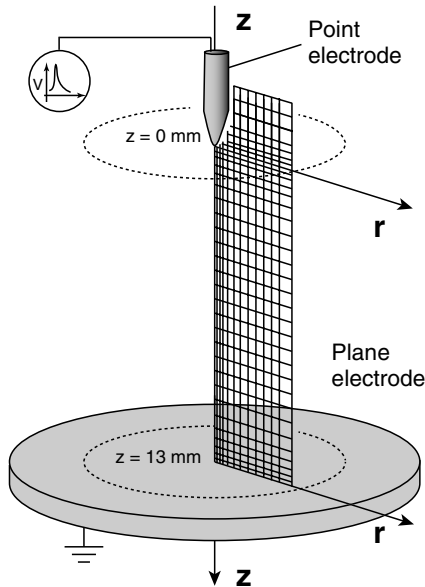


Figure 2. Computation domain.

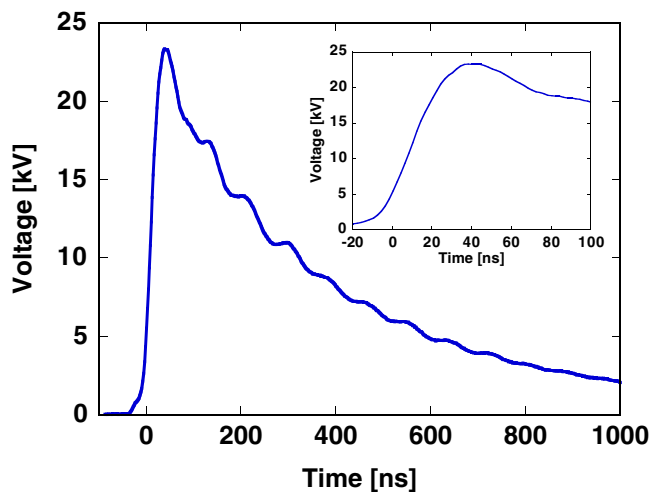
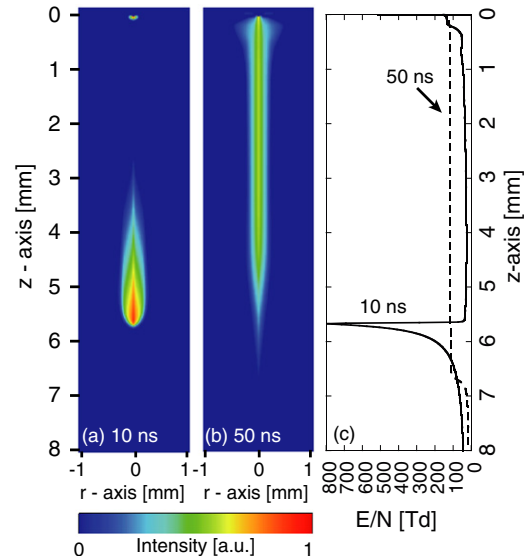
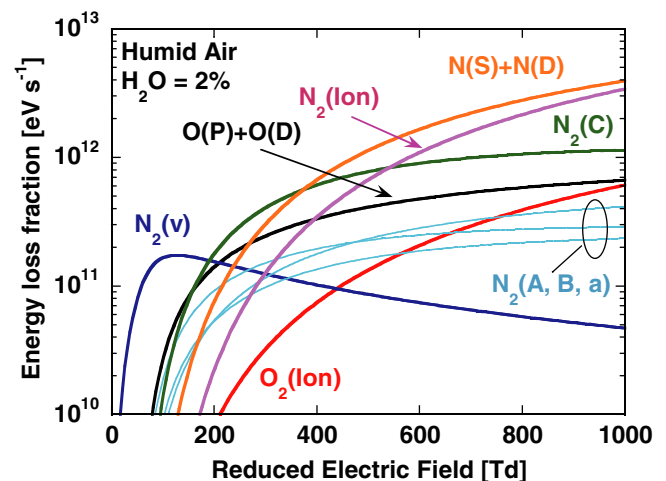


Figure 3. Applied voltage input in this simulation. The voltage waveform was obtained from previous experiments [49].

into the mechanism of discharge energy transfer. Based on this consideration, our simulation model includes the fast gas heating model proposed by Popov [1]. Popov [1] calculated the energy stored each of the internal modes of molecules and atoms and simulated the increase in the gas temperature during the discharge. The enthalpies of reactions that involve excited molecules are calculated in an analogous approach as that of Popov [1]. Other reactions involving molecular ground states are calculated using standard enthalpies of formation listed in table 3. The standard enthalpies of formation for excited species are estimated by the corresponding threshold energies listed in table 2. When the reaction products have a vibrational mode, e.g. when the reaction $\text{N}_2(a'^1\Sigma_u^-) + \text{H}_2\text{O} \rightarrow \text{N}_2(v) + \text{OH} + \text{H}$ proceeds, the excess heat of the reaction is distributed to both the vibrational energy of $\text{N}_2(v)$ and the exothermic energy. The distribution ratio differs depending the specifics of each reaction [47, 48] and most of them were

Figure 4. Cross sectional views of instantaneous flux of photons emitted from $\text{N}_2(C^3\Pi_u)$ for a horizontal line of sight in $\text{O}_2(20\%)/\text{N}_2$ discharge at (a) $t = 10$ ns, (b) $t = 50$ ns and (c) the corresponding axial distribution of reduced electric field (E/N) at each time.Figure 5. The fractions of energy partitioned into the excitation, ionization, and dissociation of molecules in $\text{H}_2\text{O}(2\%)/\text{air}$.

not studied. Therefore, in this paper, only 70% of the reaction enthalpy is assumed to be partitioned into translational and rotational modes, with the remainder assumed to be directed into vibrational modes. A list of the relevant reactions and their rate coefficients are given in [27].

Gas heating by ion–molecule reactions may be effective at high E/N conditions. Popov [1] showed that ion–molecule reactions are a major process for heating gas at $E/N > 400$ Td. However, in an atmospheric-pressure streamer discharge, such high electric field, such as $E/N > 400$ Td, occur only at the tip of the streamer head and the streamer rapidly pass through the discharge gap [49]. Instead, the secondary streamer, which $E/N \approx 110$ Td, can produce a large number of radicals and can initiate subsequent chemical reactions [45]. Therefore, the effect of gas heating by ion–molecule reaction is estimated to be negligibly small and is ignored in our simulation.

Table 3. Standard enthalpy of formation for species considered in the H₂O/Air reaction mechanism at 298 K [65, 64, 66].

Species	ΔH_f (kJ mol ⁻¹)
N ₂	0.0
O ₂	0.0
H ₂	0.0
H ₂ O	-241.83
N(⁴ S)	472.68
N(² D)	702.60
O(³ P)	249.17
O(¹ D)	438.92
H	218.00
OH	38.99
O ₃	142.67
NO	90.29
NO ₂	33.1
N ₂ O	82.05
H ₂ O ₂	-136.11
HO ₂	2.09
HNO	99.58
HNO ₂	-76.73
HNO ₃	-134.31

Table 4. V-T and V-V processes considered in the simulation model. v and w are vibrational quantum numbers.

V-T processes
$O_2(v) + O_2(0) \rightleftharpoons O_2(v-1) + O_2(0)$
$N_2(v) + N_2(0) \rightleftharpoons N_2(v-1) + N_2(0)$
$O_2(v) + N_2(0) \rightleftharpoons O_2(v-1) + N_2(0)$
$N_2(v) + O_2(0) \rightleftharpoons N_2(v-1) + O_2(0)$
$H_2O(0\ 1\ 0) + H_2O(0\ 0\ 0) \rightleftharpoons H_2O(0\ 0\ 0) + H_2O(0\ 0\ 0)$
$H_2O(1\ 0\ 0) + H_2O(0\ 0\ 0) \rightleftharpoons H_2O(0\ 0\ 0) + H_2O(0\ 0\ 0)$
$H_2O(0\ 0\ 1) + H_2O(0\ 0\ 0) \rightleftharpoons H_2O(0\ 0\ 0) + H_2O(0\ 0\ 0)$
$O_2(1) + O(P) \rightleftharpoons O_2(0) + O(P)$
$N_2(1) + N(S) \rightleftharpoons N_2(0) + N(S)$
V-V processes
$O_2(v) + O_2(w) \rightleftharpoons O_2(v-1) + O_2(w+1)$
$N_2(v) + N_2(w) \rightleftharpoons N_2(v-1) + N_2(w+1)$
$N_2(v) + O_2(w) \rightleftharpoons N_2(v-1) + O_2(w+1)$
$O_2(1) + H_2O(0\ 0\ 0) \rightleftharpoons O_2(0) + H_2O(0\ 1\ 0)$
$N_2(1) + H_2O(0\ 0\ 0) \rightleftharpoons N_2(0) + H_2O(0\ 1\ 0)$

The vibrational kinetics are modelled using a state-to-state model [23, 50]. The vibration-to-translation (V-T) and vibration-to-vibration (V-V) transitions considered in the simulation are listed in table 4. The vibrational modes of H₂O (v_1, v_2, v_3) are the equilibrated stretching (v_1, v_3) and bending (v_2) modes. Multi-quantum processes ($\Delta v \geq 2$) for the N₂-N₂ and O₂-N₂ systems [51, 52] are not considered because they are negligible at low-temperatures (e.g. below 1000 K). The rate coefficients for the direct and reverse transitions are related by the principle of detailed balance [10]. For O₂(v) and N₂(v), only $v \leq 8$ is considered because highly excited molecules ($v > 8$) have little influence on the V-T and V-V processes. The detailed kinetics and calculation method for the rate coefficients of the V-T and V-V reactions are detailed in [23]. In dry air, effects of vibrational relaxation on the gas temperature can be ignored because the time constant for vibrational relaxation is larger than that for particle diffusion, which is itself greater than the order of ms [53–55].

However, in humid air, the vibrational relaxation rate is greatly accelerated by interactions between O₂(v) and H₂O(v), and may serve to increase the gas temperature just after the discharge [23, 24].

2.3. Model of gas fluid

In this paper, the two-dimensional axis-symmetric Euler equation is solved to simulate neutral gas flow as follows:

$$\frac{\partial}{\partial t}(rQ) + \frac{\partial}{\partial r}(rF) + \frac{\partial}{\partial z}(rG) = S, \quad (6)$$

$$Q = \begin{pmatrix} \rho \\ \rho v_r \\ \rho v_z \\ \rho E \end{pmatrix}, \quad F = \begin{pmatrix} \rho v_r \\ \rho v_r^2 + p \\ \rho v_r v_z \\ \rho H v_r \end{pmatrix},$$

$$G = \begin{pmatrix} \rho v_z \\ \rho v_r v_z \\ \rho v_z^2 + p \\ \rho H v_z \end{pmatrix}, \quad S = \begin{pmatrix} 0 \\ p \\ 0 \\ S_\epsilon \end{pmatrix},$$

$$E = \frac{v_r^2 + v_z^2}{2} + \frac{1}{\gamma - 1} \frac{p}{\rho}, \quad H = \frac{v_r^2 + v_z^2}{2} + \frac{\gamma}{\gamma - 1} \frac{p}{\rho}.$$

Here, Q is the vector of conserved variables, F and G are the vectors of fluxes, and S is the vector of source terms, ρ is the gas density, v_r and v_z are the gas velocities in the radial and axial directions, E is the gas energy per unit mass, p is the gas pressure, H is the gas enthalpy per unit mass, S_ϵ is the energy source term, and γ is the ratio of specific heat (assumed to be 1.4). These equations (6) are closed by the ideal gas state equation. The gas heating model considered in section 2.2 is coupled to (6) by inputting the reaction enthalpies into S_ϵ . Equation (6) is solved using the symmetric-TVD method with the minmod limiter function [41]. The gliding condition is applied for the neutral gas velocity field on the electrode surfaces. The temperature at the surface of the electrode is assumed to remain at ambient temperature. We have applied similar conditions to those discussed in detail by Kacem *et al* [56] for the boundary conditions when solving the hydrodynamic equations of a compressible fluid. The same kind of two-dimensional axis-symmetric Euler code can be found in [26].

3. Results

3.1. Streamer propagation

Figure 6 shows the streak pictures of (a) the reduced electric field, E/N , (b) the electron density, n_e , (c) the gas density, N , (d) the gas temperature, T , and (e) the gas pressure, p , in H₂O(2%)/air. The streak pictures plot the time-dependent distribution of each value along the axis of symmetry. Figures 6(a) and (b) show that the streamer starts to propagate at an applied potential of 5 kV and reaches the plane at about $t = 20$ ns. After the arrival of the primary streamer at the plane, the secondary streamer starts to extend. The E/N at the streamer head is approximately 800 Td (1 Td = 10^{-17} V cm²)

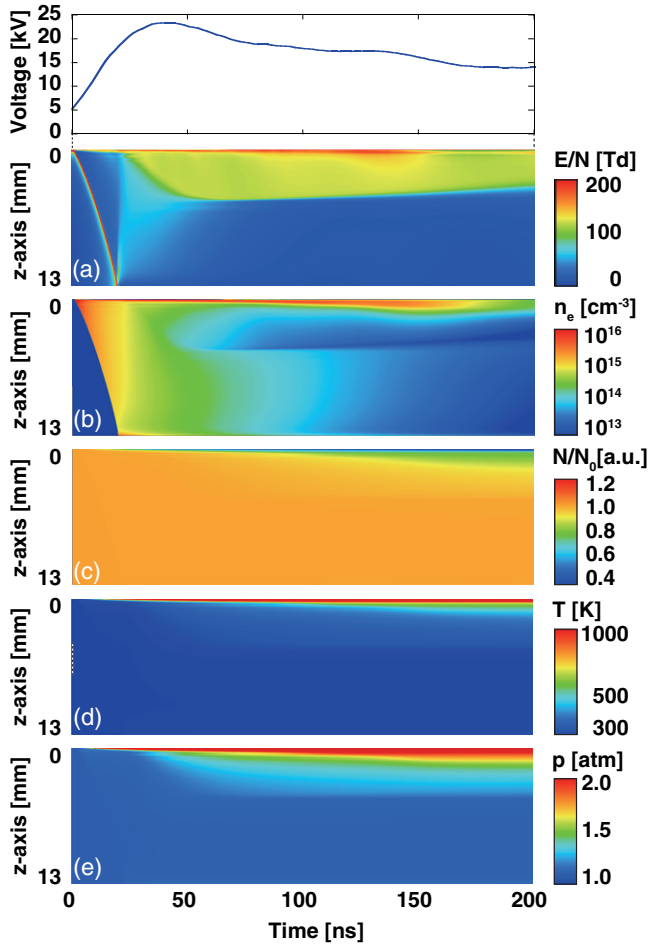


Figure 6. Simulated streak images for (a) the reduced electric field, E/N , (b) the electron density, n_e , (c) the normalized gas density, N/N_0 , (d) the gas temperature, T , and (e) the gas pressure, p , in $\text{H}_2\text{O}(2\%)/\text{air}$.

and remains almost constant when the streamer propagates to the plane cathode regardless of the humidity. The E/N in the secondary streamer is approximately 120 Td in $\text{H}_2\text{O}(2.0\%)/\text{air}$ and it slightly decreases in $\text{H}_2\text{O}(0.1\%)/\text{air}$ because of the electronegative character of H_2O [27]. The n_e just above the plane around $t = 20\text{--}40$ ns in figure 6(b) increases because of cathode fall effects. The thickness of the cathode fall region is 0.2 mm above the plane and E/N reaches a maximum of 1500 Td. Electrons produced by the ionization of N_2 and O_2 are consumed by dissociative recombination of N_2 : $\text{N}_2^+ + e^- \rightarrow 2\text{N}(^4\text{S})$ and three-body electron attachment of O_2 : $\text{O}_2 + \text{O}_2 + e^- \rightarrow \text{O}_2 + \text{O}_2^-$ in the streamer channel. The dissociative attachment of O_2 : $\text{O}_2 + e^- \rightarrow \text{O}(^3\text{P}) + \text{O}^-$ is a major electron-decay process in the secondary streamer. Primary and secondary streamers were simulated and compared with experimental streak camera in [28–30]. We also simulated the streak pictures in our previous paper [45] and successfully reproduced the experimentally measured acceleration of the primary streamer, and the ratio of the discharge emissions from primary and secondary streamer. The hydrodynamic parameters of the gas N , T , and p change gradually from just below the point anode. The high E/N and n_e around the point anode lead to positive feedback, which increases the

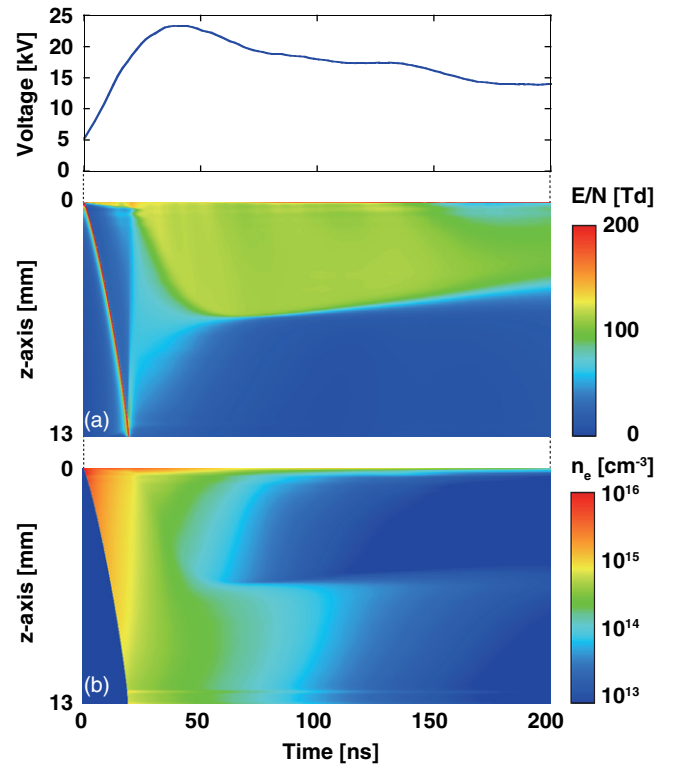


Figure 7. Simulated streak images for (a) the reduced electric field, E/N and (b) the electron density, n_e , in $\text{H}_2\text{O}(2\%)/\text{air}$. The gas density N of E/N is assumed as constant. Reprinted with permission from [45]. © 2012 IOP Publishing.

gas temperature and pressure and decreases the density. The normalized gas density decreases to a minimum of 0.5, the gas temperature increases to a maximum of 2000 K, and the gas pressure increases to a maximum of 4 atm just below the point electrode. Although E/N and n_e decrease from $t = 150$ ns as the applied potential decreases, the gas density continues to decrease. The time constant of a decrease in the gas density may change according to the condition, especially to the radius of the streamer channel [28]. We have already showed in our previous paper [27] that the absolute diameter of the simulated streamer channel are slightly thinner than obtained by experiments. It may influence the results in this paper. The detailed mechanism of gas heating in the discharge is explained in section 3.3.

The effect of gas heating on E/N and n_e are analysed by comparison with simulations in which the gas density is assumed to be constant. Figure 7 shows streak pictures of E/N and n_e with constant gas density [49]. The remarkable differences between the results in figures 6 and 7 are the length of the secondary streamer and the different E/N behaviour in the secondary streamer. The secondary streamer plays an important role in radical production [27], so changing N may affect the radical production. Some researchers have put forth the necessity of solving the neutral gas flow equations during the voltage pulse. Kacem *et al* [56] simulated the gas heating and the corresponding gas expansion generated by a dc point-to-plane streamer discharge under atmospheric pressure. In their simulation, the N of E/N is assumed to be constant because the gas inertia can be estimated to be about 100 ns.

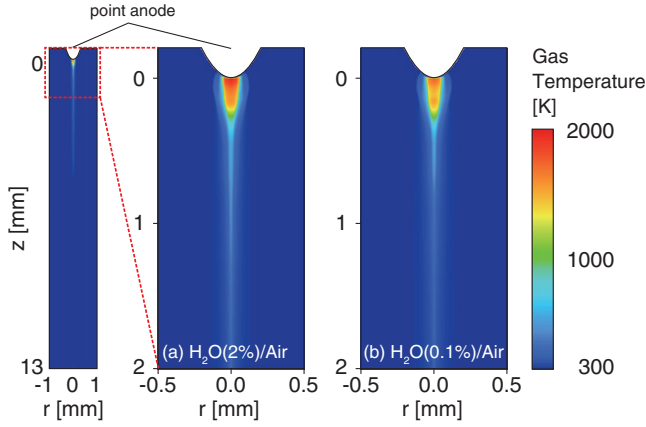


Figure 8. Simulated gas temperature in (a) $\text{H}_2\text{O}(2\%)/\text{air}$ and (b) $\text{H}_2\text{O}(0.1\%)/\text{air}$ at $t = 200$ ns.

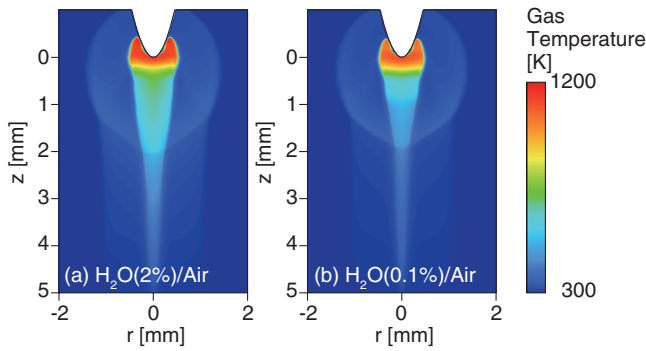


Figure 9. Simulated gas temperature in (a) $\text{H}_2\text{O}(2\%)/\text{air}$ and (b) $\text{H}_2\text{O}(0.1\%)/\text{air}$ at $t = 3 \mu\text{s}$.

Tholin and Bourdon [26] assume the N of E/N to be constant because they estimate the influence on transport coefficients and rate coefficients in the source terms to be small. However, they did not estimate the extremely high gas temperature and pressure around the point electrode as shown in figure 6. The effect of varying N of E/N on the discharge kinetics must be verified by further experiments.

3.2. Simulations of gas temperature and comparison with experimental results

Figure 8 shows the two-dimensional distributions of the gas temperature at $t = 200$ ns in (a) $\text{H}_2\text{O}(2\%)/\text{air}$ and (b) $\text{H}_2\text{O}(0.1\%)/\text{air}$. The gas temperature just below the point anode reaches 2000 K and there are no remarkable differences between the gas temperature distributions in $\text{H}_2\text{O}(2\%)/\text{air}$ and $\text{H}_2\text{O}(0.1\%)/\text{air}$. Figure 9 shows the two-dimensional distributions of the gas temperature at $t = 3 \mu\text{s}$ in (a) $\text{H}_2\text{O}(2\%)/\text{air}$ and (b) $\text{H}_2\text{O}(0.1\%)/\text{air}$. The high-gas-temperature region spreads around the point anode and shock waves propagate spherically from there. The shock waves were already observed in our previous experimental results [54]. After initiation of the shock wave, the maximum of the gas temperature decreases to 1200 K. This is because a portion of the thermal energy stored in front of the point anode is transported by the pressure wave outside of the initial heated region [56]. Streamer discharge induced shock waves have

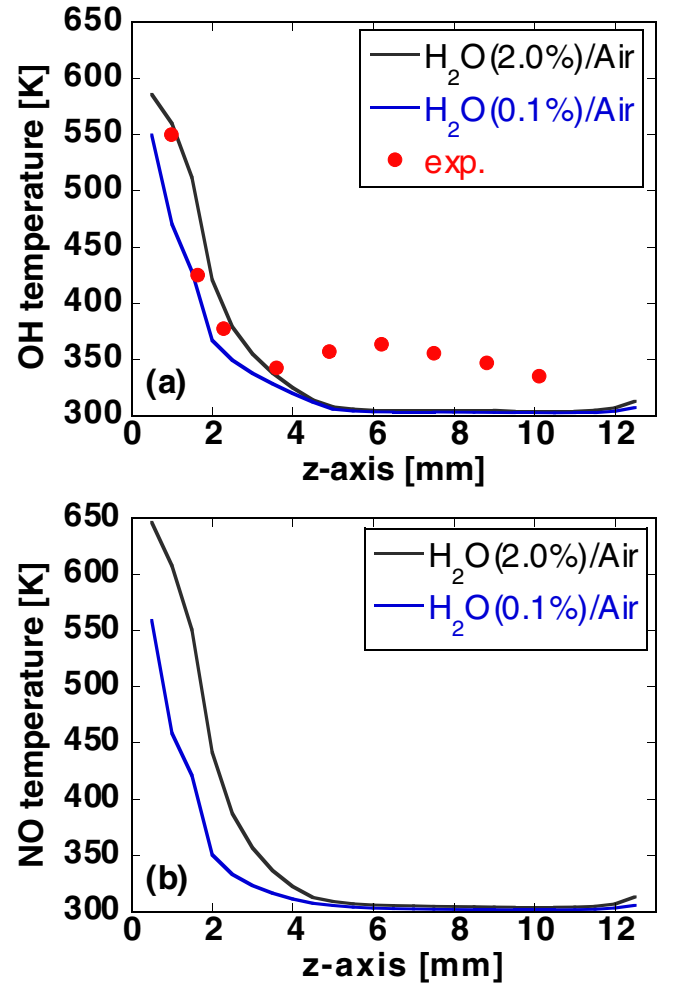


Figure 10. Axial distribution of simulated gas temperature weighted by (a) OH radical density distribution and (b) NO molecular density at $t = 3 \mu\text{s}$. The red circles in (a) are the plot of our previous experimental results that were measured in $\text{H}_2\text{O}(2.3\%)/\text{air}$ at $20 \mu\text{s}$ after the discharge [13]. Reprinted with permission from [13]. © 2011 AIP Publishing.

already been simulated in [56], and our simulation results are qualitatively in agreement with these previous studies. Comparing figures 9(a) and (b), a high-temperature region spreads and the maximum of the gas temperature increases at higher humidity. The detailed mechanism of gas heating in humid air is discussed in section 3.3.

In order to check the validity of our simulation results, the simulated gas temperatures are compared with our previous experimental results. Since it is difficult to directly measure the translational temperature, the rotational temperature is measured, and we assume that the rotational temperature instantly reaches an equilibrium state with the translational temperature. Here, the simulated temperature is compared with previously measured rotational temperatures of both NO and OH after the discharge [12, 13]. Figure 10 shows the simulated gas temperature weighted by the spatial distribution of the simulated (a) OH and (b) NO densities. The method for weighting is that the number of OH or NO produced are multiplied by the gas temperature, and they are averaged in the observation volume. The simulated temperatures are obtained

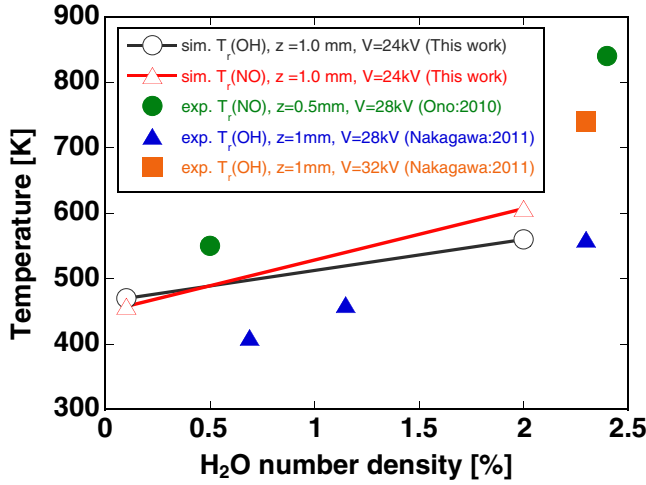


Figure 11. Comparison between simulated gas temperatures and experimentally obtained rotational temperatures of OH and NO molecules in various humidity conditions at $t = 3 \mu\text{s}$. Filled symbols correspond to experimental data: full-circle [53], full-triangle and full-square [13]. The open-circle and open-triangle data are simulated in this work.

by taking the average temperature in the observation volume ($\pi r^2 \times dz = \pi \times 8^2 \times 1 \text{ mm}^3$) at z mm from the point anode corresponding to the experiments [13]. The simulated gas temperatures below the anode at time $t = 3 \mu\text{s}$ increase with increasing humidity, as shown in figures 10(a) and (b). Points in figure 10(a) show the rotational temperature of OH obtained from the experiment, where the applied voltage was 28 kV in $\text{H}_2\text{O}(2.3\%)/\text{air}$ at $t = 20 \mu\text{s}$ [13]. Although the experimental conditions were slightly different from the simulation, the experimental and simulation results are in qualitative agreement for the high temperature near the point anode and the flat distribution near the plane cathode.

Figure 11 illustrates the effects of humidity on the simulated gas temperature near the point anode just after the discharge. The experimentally obtained rotational temperatures [53, 13] are also plotted in figure 11. The experimental and simulated results show the same trend that gas temperature increases with increasing humidity. In addition, the measured rotational temperature of NO is higher than that of OH. In $\text{H}_2\text{O}(2.0\%)/\text{air}$, the simulated NO temperature is about 50 K higher than the simulated OH temperature. This molecular dependence of the rotational temperatures is caused by differences in their radial distributions. Figures 12(a) and (b) show the two-dimensional distributions of NO and OH molecules at $t = 200 \text{ ns}$. Figure 12(c) shows the radial distribution of these two molecules between $z = 0.5\text{--}1.5 \text{ mm}$. The radial distributions of the OH and NO molecules in figure 12(c) are normalized by each value on the axis of symmetry. The half width of the radial distribution of OH is wider than that of NO. This is because the mechanisms for NO and OH production are different. OH is mainly produced by H_2O dissociation reactions with $\text{O}(^1\text{D})$ and $\text{N}_2(a'^1\Sigma_u^-)$ [27], while NO is primarily produced by reaction of $\text{N}(^4\text{S}, ^2\text{D})$ with O_2 [57, 58]. Since the threshold energy needed for $\text{N}(^4\text{S}, ^2\text{D})$ radical production is higher than that of $\text{O}(^1\text{D})$ and $\text{N}_2(a'^1\Sigma_u^-)$, NO production requires a higher E/N

than for OH production. Therefore the NO density peaks at the axis of symmetry in the radial distribution and the half width of NO is thinner than that of OH. On the other hand, the peak of the OH density is offset from the axis of symmetry in the radial distribution because the product OH is rapidly consumed by the $\text{OH} + \text{O}(\text{P})$ and $\text{OH} + \text{OH} + \text{M}$ reactions [27]. Figure 13 shows two-dimensional distributions of the (a) OH and (b) NO densities and (c) the radial distributions of OH and NO densities and the gas temperature at $t = 3 \mu\text{s}$. The high-gas-temperature region spreads spherically as the shock wave expands, as compared with the results in figure 12. The radial distributions of the OH and NO densities also change according to the gas expansion and proceeding reactions. The results show that the radial distributions of OH and NO are different from that of the gas temperature. Because the NO radial distribution is thinner than that of OH, the NO rotational temperature is higher than for OH. Thus, the NO rotational temperature corresponds to the gas temperature near the centre of the streamer channel, as shown in figure 12(c). Parra-Rojas *et al* [59] shows different gas temperatures measured with two different species, $\text{N}_2^+(B^2\Sigma_u^+)$ and $\text{N}_2^+(B^3\Pi_g)$. In [59], it is explained that the differences can be principally caused by the spatial distributions of $\text{N}_2^+(B^2\Sigma_u^+)$ and $\text{N}_2^+(B^3\Pi_g)$. Our simulation results may support their conclusion.

3.3. Mechanism of gas heating

3.3.1. Electron-to-molecule energy transfer. Figure 14 shows the time variation of the electron energy loss $\mathcal{E}_{\text{loss}}$ by electron-impact collisions in table 2. The $\mathcal{E}_{\text{loss}}$ is calculated as follows,

$$\mathcal{E}_{\text{loss}} = \sum_k \left(\epsilon_k \int_V [M][n_e] f_k dV \right), \quad (7)$$

where ϵ_k is the threshold energy of the k th reaction, $[M]$ is the number density of N_2 , O_2 , or H_2O , $[n_e]$ is the electron number density, f_k is the rate coefficient of the k th reaction, and dV is the calculation volume. The electron energy loss through the production of $\text{N}_2(v)$ is also shown in figure 14. Figure 14 shows that a large amount of energy is consumed in the production of $\text{N}_2(v)$. The total amount of electron energy loss is $147.5 \mu\text{J}$ in $\text{H}_2\text{O}(0.1\%)/\text{air}$ and $130.4 \mu\text{J}$ in $\text{H}_2\text{O}(2\%)/\text{air}$. Figure 15 shows the fraction of the total electron energy loss attributed to each reaction in table 2. Over 70% of the electron energy is consumed by the production of $\text{N}_2(v)$. The rest of the electron energy is used to produce electronically excited N_2 and in the dissociation reactions of O_2 and N_2 . About 3% of the total electron energy is consumed by $\text{H}_2\text{O}(v_1, v_2, v_3)$ in $\text{H}_2\text{O}(2\%)/\text{air}$, which instead is consumed by $\text{N}_2(v)$ in $\text{H}_2\text{O}(0.1\%)/\text{air}$.

3.3.2. Energy relaxation of excited molecules. Here, the gas heating processes resulting from energy relaxation of the discharge products are investigated. Figure 16 shows the total amount of the energy released from each reaction up to $t = 3 \mu\text{s}$. The reaction numbering scheme in figure 16 corresponds with reactions listed in table 5. Figure 16 indicates that the main contributors to the fast gas heating are $\text{O}(^1\text{D})$ and

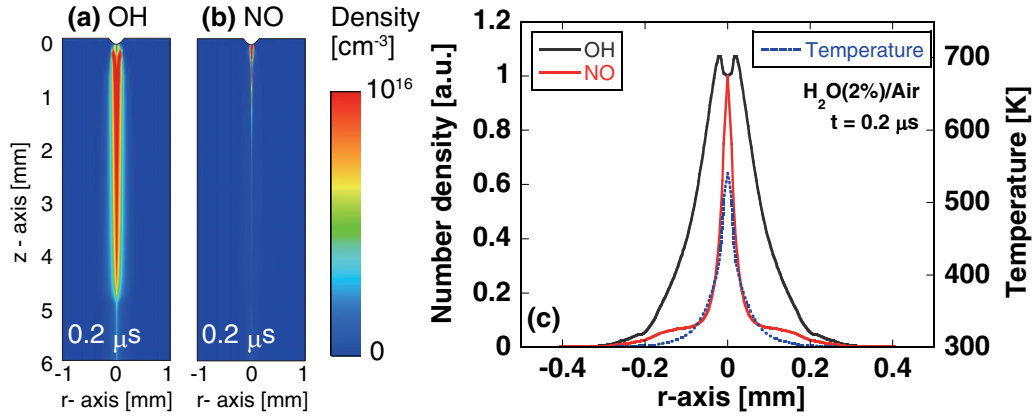


Figure 12. Cross sectional views of (a) OH and (b) NO densities at $t = 0.2 \mu\text{s}$. (c) Radial distribution of OH and NO densities and gas temperature at $z = 0.5-1.5 \text{ mm}$ at $t = 0.2 \mu\text{s}$ in $\text{H}_2\text{O}(2\%)/\text{air}$.

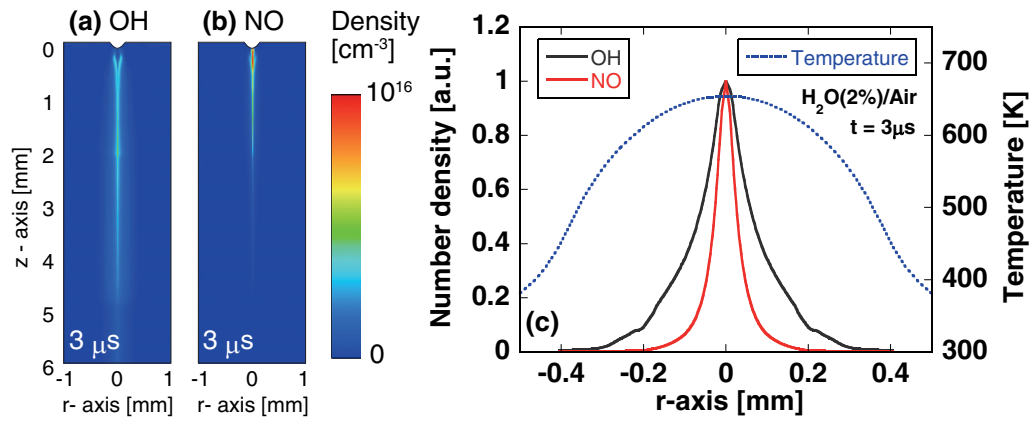


Figure 13. Cross sectional views of (a) OH and (b) NO densities at $t = 3 \mu\text{s}$. (c) Radial distribution of OH and NO densities and gas temperature at $z = 0.5-1.5 \text{ mm}$ at $t = 3 \mu\text{s}$ in $\text{H}_2\text{O}(2\%)/\text{air}$.

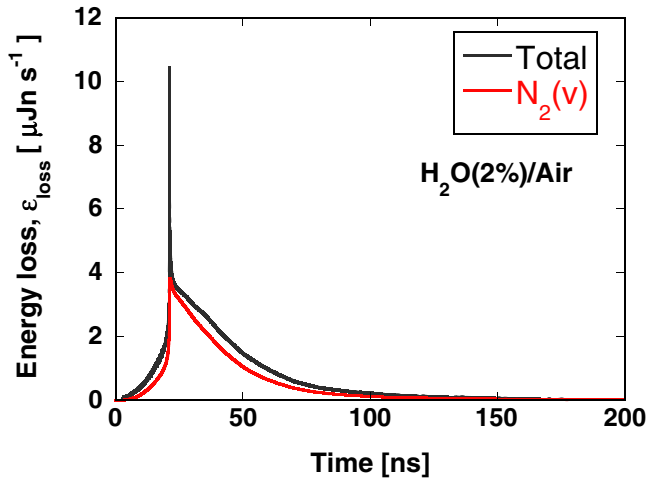


Figure 14. Energy loss of electrons by the electron-impact collision processes listed in table 2 in $\text{H}_2\text{O}(2\%)/\text{air}$.

$\text{N}_2(B, C)$ quenching reactions and electron-impact collision-induced O_2 dissociation reactions. Popov [1] theoretically show that the (R1), (R2), (R3), (R4), and (R6) reactions are the major gas heating processes under $E/N < 200 \text{ Td}$ conditions. On the other hand, the effect of N_2 electron-impact dissociation reaction (R12), which is proposed to be the major gas heating

process for $E/N > 400 \text{ Td}$ conditions, is seen to only be a minor channel in this simulation. These results indicate that gas heating mainly occurs in the secondary streamer whose E/N is about 110–120 Td. Reactions (R9), (R10), (R13), (R14) and (R15) include water related radicals such as H and HO_2 which contribute greatly to OH radical production [27]. This result indicates that OH formation processes increase the gas temperature in humid air. The energy released from $\text{O}(^1\text{D})$ quenching (R1) in $\text{H}_2\text{O}(0.1\%)/\text{air}$ is remarkably larger than that in $\text{H}_2\text{O}(2\%)/\text{air}$ because the quenching of $\text{O}(^1\text{D})$ can also occur by reaction (R14) in $\text{H}_2\text{O}(2\%)/\text{air}$. The branching $\text{O}(^1\text{D})$ reactions result in an overall decrease in $\text{O}(^3\text{P})$ production instead of increasing OH production in humid air.

Figure 17 shows the time variation of the molecular energies obtained from the multiplication of the number of each product species and its corresponding standard enthalpy of formation. Figure 17(a) shows that little vibrational relaxation of $\text{N}_2(v)$ is seen up to $t = 3 \mu\text{s}$ in both humid and dry air. $\text{O}(^3\text{P})$ receives a large amount of energy from the electronically excited molecules and atoms used in $\text{O}(^3\text{P})$ production through reactions (R1), (R2), (R3), (R4) and (R6). A portion of the energy stored in $\text{N}_2(v)$ in $\text{H}_2\text{O}(0.1\%)/\text{air}$ is instead partitioned into $\text{H}_2\text{O}(v_1, v_2, v_3)$ in $\text{H}_2\text{O}(2\%)/\text{air}$. The energy contained in $\text{O}(^3\text{P})$ in $\text{H}_2\text{O}(2\%)/\text{air}$ is decreased from that in $\text{H}_2\text{O}(0.1\%)/\text{air}$ because of the production of OH by $\text{O}(^3\text{P})$ (R10) and the

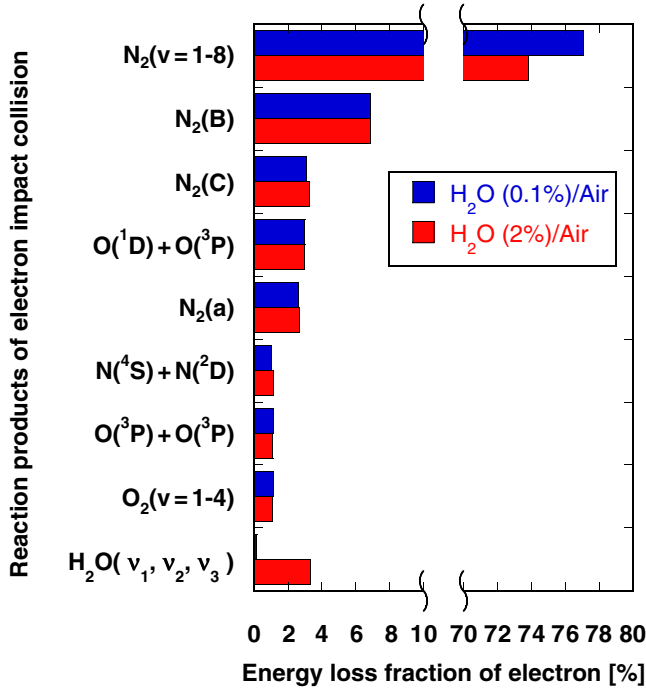


Figure 15. Energy loss fractions of electrons by the electron-impact collision processes listed in table 2.

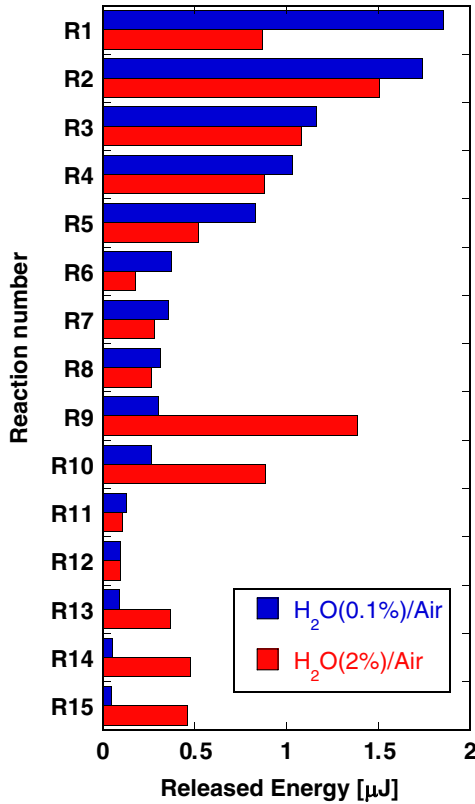


Figure 16. Contribution of each reactions to gas heating up to $3 \mu\text{s}$ for $V = 24 \text{ kV}$. These values are calculated over the whole discharge area. The reaction numbering scheme corresponds with table 5.

$\text{O}(^1\text{D})$ branching reaction (R14). Figure 17(b) shows the time variation of the energy stored in $\text{O}_2(v)$, $\text{H}_2\text{O}(v_1, v_2, v_3)$, and electronically excited N_2 on a much smaller energy scale than figure 17(a). Figure 17(b) shows that nearly all

Table 5. Main reactions that contribute to gas heating over the first $3 \mu\text{s}$ in humid air. The complete set of reactions is given in [27]. ϵ_R is a enthalpy of reaction.

Reaction	ϵ_R (eV)
(R1) $\text{O}(^1\text{D}) + M \rightarrow \text{O}(^3\text{P}) + M, M = \text{O}_2(v), \text{N}_2(v)$	1.37
(R2) $\text{N}_2(B) + \text{O}_2 \rightarrow \text{N}_2(v) + \text{O}(^3\text{P}) + \text{O}(^3\text{P})$	1.53
(R3) $\text{N}_2(C) + \text{O}_2 \rightarrow \text{N}_2(v) + \text{O}(^3\text{P}) + \text{O}(^3\text{P})$	4.11
(R4) $\text{O}_2 + e^- \rightarrow \text{O}(^1\text{D}) + \text{O}(^3\text{P}) + e^-$	1.26
(R5) $\text{O}(^3\text{P}) + \text{O}_2 + M \rightarrow \text{O}_3 + M, M = \text{O}_2(v), \text{N}_2(v)$	0.77
(R6) $\text{N}_2(a) + \text{O}_2 \rightarrow \text{N}_2(v) + \text{O}(^3\text{P}) + \text{O}(^1\text{D})$	0.89
(R7) $\text{O}(^3\text{P}) + \text{NO} + \text{N}_2 \rightarrow \text{NO}_2 + \text{N}_2(v)$	2.22
(R8) $\text{O}_2 + e^- \rightarrow \text{O}(^1\text{P}) + \text{O}(^3\text{P}) + e^-$	0.78
(R9) $\text{H} + \text{O}_2 + M \rightarrow \text{HO}_2 + M, M = \text{O}_2(v), \text{N}_2(v)$	1.57
(R10) $\text{O}(^3\text{P}) + \text{HO}_2 \rightarrow \text{OH} + \text{O}_2(v)$	1.54
(R11) $\text{N}(^2\text{D}) + \text{O}_2 \rightarrow \text{NO} + \text{O}(^1\text{D})$	1.76
(R12) $\text{N}_2 + e^- \rightarrow \text{N}(^4\text{S}) + \text{N}(^2\text{D}) + e^-$	0.90
(R13) $\text{OH} + \text{O}(^3\text{P}) \rightarrow \text{O}_2(v) + \text{H}$	0.51
(R14) $\text{O}(^1\text{D}) + \text{H}_2\text{O} \rightarrow \text{OH} + \text{OH}$	0.86
(R15) $\text{N}_2(a) + \text{H}_2\text{O} \rightarrow \text{N}_2(v) + \text{OH} + \text{H}$	2.26

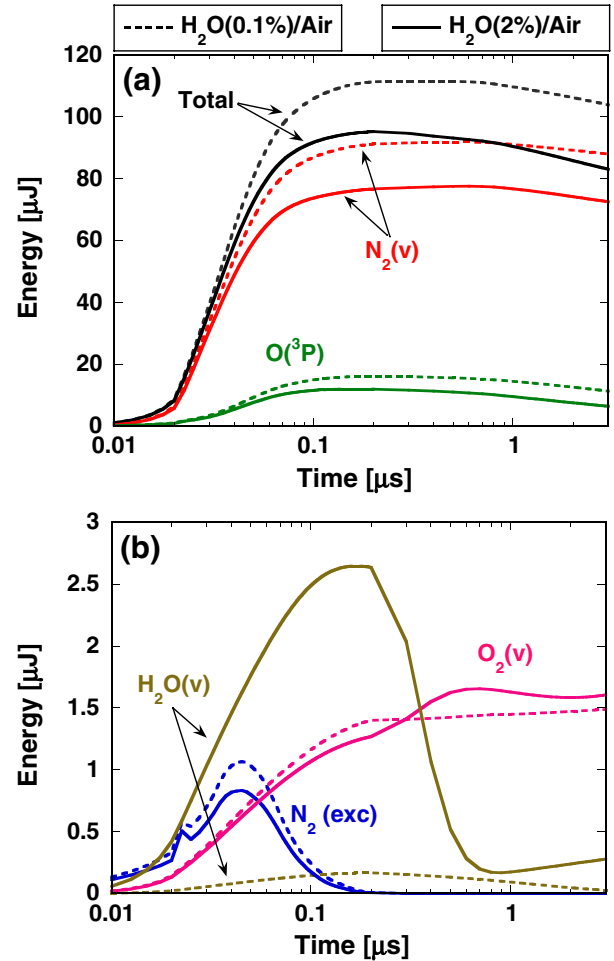


Figure 17. Simulated temporal variation of the sequestered energy in discharge products for (---) $\text{H}_2\text{O}(0.1\%)/\text{air}$ and in (—) $\text{H}_2\text{O}(2\%)/\text{air}$. Note the different energy scales in (a) and (b). $\text{N}_2(\text{exc})$ means electronically excited states of N_2 .

the energy stored in electronic energy states of N_2 relaxes during the discharge pulse. Humidity has little effect on the electronically excited species of N_2 and $\text{O}_2(v)$. On the other hand, a relatively large amount of energy is stored in

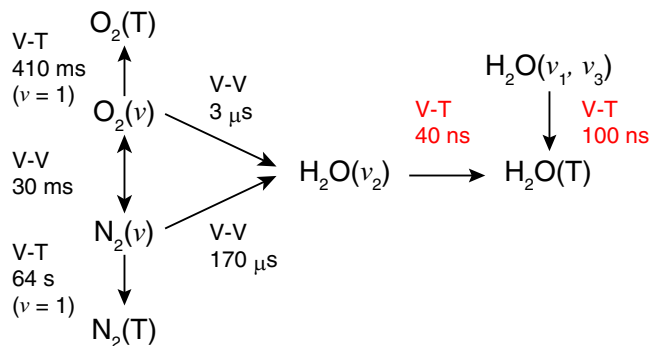


Figure 18. Time constants for vibrational energy transfer in $\text{H}_2\text{O}(2\%)/\text{air}$ at a temperature $T = 300$ K. These time constants are calculated by the rate constants in [60] for O_2 -VT and N_2 -VT, [10, 61] for H_2O -VT, [10] for O_2 - N_2 -VV, [62] for N_2 - H_2O -VV, and [63] for O_2 - H_2O -VV.

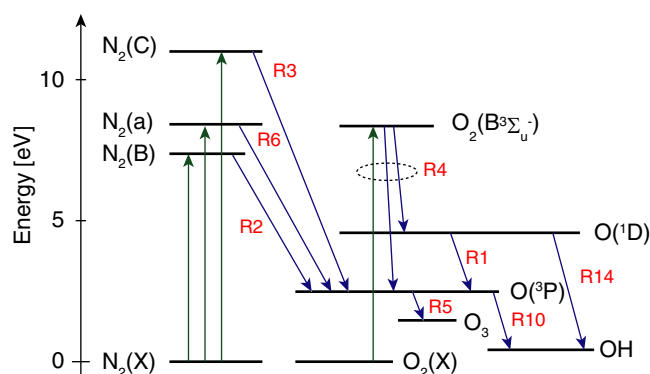


Figure 19. Diagram of energy relaxation processes of discharge products.

$\text{H}_2\text{O}(v_1, v_2, v_3)$ and it rapidly relaxes in $\text{H}_2\text{O}(2\%)/\text{air}$. This is caused by the V-T relaxation of H_2O . Figure 18 shows a diagram of V-V and V-T relaxation in $\text{H}_2\text{O}(2\%)/\text{air}$ at ambient temperature. The fast H_2O - H_2O V-T processes contribute to the fast gas heating. On the other hand, vibrational relaxation of $\text{N}_2(v)$ and $\text{O}_2(v)$ barely commence by $t = 3 \mu\text{s}$ both in humid and dry air as shown in figure 17. However, since $\text{N}_2(v)$ still has a large amount of stored energy at $t = 3 \mu\text{s}$, accelerated vibrational relaxation via V-V processes for O_2 - H_2O and N_2 - H_2O may affect subsequent gas heating and gas expansion [23].

Figure 19 shows a diagram of energy relaxation processes between discharge products. The vertical axis corresponds to the enthalpy of formation of each molecule or atom. The energy stored in electronically excited N_2 can be used to produce $\text{O}(^3\text{P})$ through reactions (R2), (R3) and (R6). In the same manner, the production of $\text{O}(^3\text{P})$ can occur by the oxygen dissociation reaction, (R4). $\text{O}(^1\text{D})$, which is also produced by (R4), is quenched to $\text{O}(^3\text{P})$ through (R1) in dry air. The energy stored in $\text{O}(^3\text{P})$ is gradually released to form O_3 after the discharge. Since the O_3 enthalpy of formation is lower than that of $\text{O}(^3\text{P})$, the energy difference is released through (R5). On the other hand, in humid air, about half of the energy stored in $\text{O}(^1\text{D})$ and a part of the energy stored in $\text{O}(^3\text{P})$ are used to produce OH with accompanying exothermic energy release. As a result, humid air is more

easily heated than dry air by an atmospheric-pressure streamer discharge.

4. Conclusion

The detailed mechanism of fast gas heating in an atmospheric-pressure streamer discharge and the effects of humidity were discussed. The following conclusions were drawn from this study.

- Fast gas heating in an atmospheric-pressure streamer discharge induces high-temperature and high-pressure conditions just below the anode and subsequent decrease in gas density. The decrease in gas density begets an increase in E/N and n_e in the secondary streamer.
- The fast gas heating during the discharge occurs mainly due to electron-impact dissociation reactions of O_2 molecules and to processes that quench electronically excited $\text{N}_2(B^3\Pi_g, C^3\Pi_u)$ molecules and $\text{O}(^1\text{D})$ atoms.
- In humid air, V-T transitions of H_2O and the enthalpy of OH formation reactions additionally increase the gas temperature.
- Over 70% of the discharge energy is used for the production of $\text{N}_2(v)$, whereas about 1% and 3% of the energy is used to produce $\text{O}_2(v)$ and $\text{H}_2\text{O}(v)$ in $\text{H}_2\text{O}(2\%)/\text{air}$, respectively. The rest of the energy is temporally stored in $\text{O}(^3\text{P})$ and is gradually transferred to O_3 or OH.

Acknowledgments

This work was partially supported by Grant-in-Aid for Japan Society for the Promotion of Science (JSPS) Fellows and Grant-in-Aid for Science Research from the Ministry of Education, Culture, Sports, Science and Technology.

References

- [1] Popov N A 2011 Fast gas heating in a nitrogen-oxygen discharge plasma: I. Kinetic mechanism *J. Phys. D: Appl. Phys.* **44** 285201
- [2] Samukawa S, Hori M, Rauf S, Tachibana K, Bruggeman P, Kroesen G, Whitehead J C, Murphy A B, Gutsol A F and Starikovskaia S 2012 The 2012 plasma roadmap *J. Phys. D: Appl. Phys.* **45** 253001
- [3] Magne L, Blin-Simiand N, Gadonna K, Jeanney P, Jorand F, Pasquiers S and Postel C 2009 OH kinetics in photo-triggered discharges used for VOCs *Eur. Phys. J. Appl. Phys.* **47** 22816
- [4] Penetrante B M, Bardsley J N and Hsiao M C 1997 Kinetic analysis of non-thermal plasmas used for pollution control *Japan. J. Appl. Phys.* **36** 5007
- [5] Boeuf J P, Lagmich Y, Unfer Th, Callegari Th and Pitchford L C 2007 Electrohydrodynamic force in dielectric barrier discharge plasma actuators *J. Phys. D: Appl. Phys.* **40** 652
- [6] Moreau E 2007 Airflow control by non-thermal plasma actuators *J. Phys. D: Appl. Phys.* **40** 605
- [7] Mildren R P and Carman R J 2001 Enhanced performance of a dielectric barrier discharge lamp using short-pulsed excitation *J. Phys. D: Appl. Phys.* **34** L1

- [8] Fridman G, Friedman G, Gutsol A, Shekhter A B, Vasilets V N and Fridman A 2008 Applied plasma medicine *Plasma Process. Polym.* **5** 503–33
- [9] Park G Y, Park S J, Choi M Y, Koo I G, Byun J H, Hong J W, Sim J Y, Collins G J and Lee J K 2012 Atmospheric-pressure plasma sources for biomedical applications *Plasma Sources Sci. Technol.* **21** 043001
- [10] Capitelli M, Ferreira C M, Gordiets B F and Osipov A I 2000 *Plasma Kinetics in Atmospheric Gases* (Berlin: Springer)
- [11] Fridman A 2008 *Plasma Chemistry* (Cambridge: Cambridge University Press)
- [12] Ono R and Oda T 2008 Measurement of gas temperature and OH density in the afterglow of pulsed positive corona discharge *J. Phys. D: Appl. Phys.* **41** 035204
- [13] Nakagawa Y, Ono R and Oda T 2011 Density and temperature measurement of OH radicals in atmospheric-pressure pulsed corona discharge in humid air *J. Appl. Phys.* **110** 073304
- [14] Eichwald O, Yousfi M, Hennad A and Benabdessadok M D 1997 Coupling of chemical kinetics, gas dynamics, and charged particle kinetics models for the analysis of NO reduction from flue gases *J. Appl. Phys.* **82** 4781
- [15] Raizer Y P 1991 *Gas Discharge Physics* (Berlin: Springer)
- [16] Marode E, Bastien F and Bakker M 1979 A model of the streamer-induced spark formation based on neutral dynamics *J. Appl. Phys.* **50** 140
- [17] Aleksandrov N L, Kindysheva S V, Nudnova M M and Starikovskiy A Y 2010 Mechanism of ultra-fast heating in a non-equilibrium weakly ionized air discharge plasma in high electric fields *J. Phys. D: Appl. Phys.* **43** 255201
- [18] Hartmann G and Gallimberti I 1975 The influence of metastable molecules on the streamer progression *J. Phys. D: Appl. Phys.* **8** 670
- [19] Parker J G 1959 Rotational and vibrational relaxation in diatomic gases *Phys. Fluids* **2** 449
- [20] Sentman D D, Stenbaek-Nielsen H C, McHarg M G and Morrill J S 2008 Plasma chemistry of sprite streamers *J. Geophys. Res.* **113** D11112
- [21] Gordillo-Vázquez F J 2008 Air plasma kinetics under the influence of sprites *J. Phys. D: Appl. Phys.* **41** 234016
- [22] Marode E, Samson S, Djermoune D, Deschamps N and Touzeau M 1999 Time resolved temperature measurements and computation of streamer air discharge and diffusion controlled chemistry *J. Adv. Oxid. Technol.* **4** 305
- [23] Komuro A, Ono R and Oda T 2010 Kinetic model of vibrational relaxation in humid-air pulsed corona discharge *Plasma Sources Sci. Technol.* **19** 055004
- [24] Ono R and Oda T 2009 Measurement of vibrationally excited $O_2(v=6)$ in the afterglow of pulsed positive corona discharge *Plasma Sources Sci. Technol.* **18** 035006
- [25] Popov N A 2001 Investigation of the mechanism for rapid heating of nitrogen and air in gas discharges *Plasma Phys. Rep.* **27** 886
- [26] Tholin F and Bourdon A 2013 Simulation of the hydrodynamic expansion following a nanosecond pulsed spark discharge in air at atmospheric pressure *J. Phys. D: Appl. Phys.* **46** 365205
- [27] Komuro A, Ono R and Oda T 2013 Behavior of OH radicals in atmospheric-pressure streamer discharge studied by two-dimensional numerical simulation *J. Phys. D: Appl. Phys.* **46** 175206
- [28] Marode E, Djermoune D, Dessante P, Deniset C, Ségur P, Bastien F, Bourdon A and Laux C 2009 Physics and applications of atmospheric non-thermal air plasma with reference to environment *Plasma Phys. Control. Fusion* **51** 124002
- [29] Abahazem A, Merbahi N, Ducasse O, Eichwald O and Yousfi M 2008 Primary and secondary streamer dynamics in pulsed positive corona discharges *IEEE Trans. Plasma Sci.* **36** 924
- [30] Eichwald O, Ducasse O, Dubois D, Abahazem A, Merbahi N, Benhenni M and Yousfi M 2008 Experimental analysis and modelling of positive streamer in air: towards an estimation of O and N radical production *J. Phys. D: Appl. Phys.* **41** 234002
- [31] Morrow R and Lowke J J 1997 Streamer propagation in air *J. Phys. D: Appl. Phys.* **30** 614
- [32] Pancheshnyi S, Nudnova M and Starikovskii A 2005 Development of a cathode-directed streamer discharge in air at different pressures: experiment and comparison with direct numerical simulation *Phys. Rev. E* **71** 016407
- [33] Hagelaar G J M and Pitchford L C 2005 Solving the Boltzmann equation to obtain electron transport coefficients and rate coefficients for fluid models *Plasma Sources Sci. Technol.* **14** 722–33
- [34] PHELPS database (www.lxcat.laplace.univ-tlse.fr) retrieved 1 October, 2012
- [35] Itikawa Y 2006 Cross sections for electron collisions with nitrogen molecules *J. Phys. Chem. Ref. Data* **35** 31–53
- [36] Itikawa Y 2009 Cross sections for electron collisions with oxygen molecules *J. Phys. Chem. Ref. Data* **38** 1–20
- [37] Fresnet F, Baravian G, Magne L, Pasquiers S, Postel C, Puech V and Rousseau A 2002 Influence of water on NO removal by pulsed discharge in $N_2/H_2O/NO$ mixtures *Plasma Sources Sci. Technol.* **11** 152
- [38] Tochikubo F and Arai H 2002 Numerical simulation of streamer propagation and radical reactions in positive corona discharge in N_2/NO and $N_2/O_2/NO$ *Japan. J. Appl. Phys.* **41** 844–52
- [39] Luque A, Ebert U, Montijn C and Hundsdoerfer W 2007 Photoionization in negative streamers: fast computations and two propagation modes *Appl. Phys. Lett.* **90** 081501
- [40] Bourdon A, Pasko V P, Liu N Y, Célestin S, Ségur P and Marode E 2007 Efficient models for photoionization produced by non-thermal gas discharges in air based on radiative transfer and the Helmholtz equations *Plasma Sources Sci. Technol.* **16** 656–78
- [41] Ferziger J H and Perić M 1996 *Computational Methods for Fluid Dynamics* (Berlin: Springer)
- [42] Prinz H 1969 *Hochspannungsfelder* (R. Oldenbourg) [in German]
- [43] Briggs W L, Henson V E and McCormic S F 2000 *A Multigrid Tutorial* 2nd edn (Philadelphia, PA: SIAM)
- [44] Ogawa S and Aoki T 2009 GPU computing for 2-dimensional incompressible-flow simulation based on multigrid method *Trans. Japan Soc. Comp. Eng. Sci.* **2009** 20090021
- [45] Komuro A, Ono R and Oda T 2012 Numerical simulation for production of O and N radicals in atmospheric-pressure streamer discharge *J. Phys. D: Appl. Phys.* **45** 265201
- [46] Pancheshnyi S V, Starikovskaia S M and Starikovskii A Y 2001 Role of photoionization processes in propagation of cathode-directed streamer *J. Phys. D: Appl. Phys.* **34** 105
- [47] Lawrence G P 1988 State-to-state $N_2(A^3\Sigma_u^+)$ energy-pooling reactions. I. The formation of $N_2(C^3\Pi_u)$ and the Herman infrared system *J. Chem. Phys.* **88** 231
- [48] Lawrence G P 1988 State-to-state $N_2(A^3\Sigma_u^+)$ energy-pooling reactions: II. The formation and quenching of $N_2(B^3\Pi_g, v=1-12)$ *J. Chem. Phys.* **88** 6911
- [49] Komuro A, Ono R and Oda T 2013 Effects of pulse voltage rise rate on velocity, diameter and radical production of an atmospheric-pressure streamer discharge *Plasma Sources Sci. Technol.* **22** 045002
- [50] Armenise I and Capitelli M 2005 State to state vibrational kinetics in the boundary layer of an entering body in earth atmosphere: particle distributions and chemical kinetics *Plasma Sources Sci. Technol.* **14** S9
- [51] Billing G D and Fisher E R 1979 VV and VT rate coefficients in N_2 by a quantum-classical model *Chem. Phys.* **43** 395–401

- [52] Billing G D 1994 VV and VT rates in N_2 - O_2 collisions *Chem. Phys.* **179** 463–7
- [53] Ono R, Teramoto Y and Oda T 2010 Effect of humidity on gas temperature in the afterglow of pulsed positive corona discharge *Plasma Sources Sci. Technol.* **19** 015009
- [54] Ono R and Oda T 2004 Visualization of streamer channels and shock waves generated by positive pulsed corona discharge using laser schlieren method *Japan. J. Appl. Phys.* **43** 321
- [55] Ono R and Oda T 2004 Spatial distribution of ozone density in pulsed corona discharges observed by two-dimensional laser absorption method *J. Phys. D: Appl. Phys.* **37** 730
- [56] Kacem S, Ducasse O, Eichwald O, Yousfi M, Meziane M, Sarrette J P and Charrada K 2013 Simulation of expansion of thermal shock and pressure waves induced by a streamer dynamics in positive DC corona discharges *IEEE Trans. Plasma Sci.* **41** 942–7
- [57] Ramachandran B, Balakrishnan N and Dalgarno A 2000 Vibrational rotational distributions of NO formed from $N + O_2$ reactive collisions *Chem. Phys. Lett.* **332** 562
- [58] Braunstein M and Duff J W 2000 Theoretical study of the $N(^2D) + O_2(X^3\Sigma_g^-) \rightarrow O + NO$ reaction *J. Chem. Phys.* **113** 7406
- [59] Parra-Rojas F C, Passas M, Carrasco E, Luque A, Tanarro I, Simek M and Gordillo-Vázquez F J 2013 Spectroscopic diagnostics of laboratory air plasmas as a benchmark for spectral rotational (gas) temperature determination in TLEs *J. Geophys. Res.-Space Phys.* **118** 4696
- [60] Nikitin E E, Osipov A I and Umansky S Y 1994 *Vibrational-Translational Energy Exchange in Collisions of Homonuclear Diatomic Molecules (Reviews of Plasma Chemistry)* (New York/London: Consultants Bureau) chapter 1
- [61] Finzi J, Hovis F E, Panfilov V N, Hess P and Moore C B 1977 Vibrational relaxation of water vapor *J. Chem. Phys.* **67** 4053
- [62] Whitson M E and McNeal R J 1977 Temperature dependence of the quenching of vibrationally excited N_2 by NO and H_2O *J. Chem. Phys.* **66** 2696–700
- [63] Huestis D L 2006 Vibrational energy transfer and relaxation in O_2 and H_2O *J. Phys. Chem. A* **110** 6638–42
- [64] Chase M W Jr 1998 NIST-JANAF Thermochemical tables, 4th edn *J. Phys. Chem. Ref. Data* Monograph 9 1
- [65] Atkinson R, Baulch D L, Cox R A, Crowley J N, Hampson R F, Hynes R G, Jenkin M E, Rossi M J and Troe J 2004 Evaluated kinetic and photochemical data for atmospheric chemistry: I. Gas phase reactions of O_x , HO_x , NO_x and SO_x species *Atoms. Chem. Phys.* **4** 1461
- [66] Manion J A *et al* 2008 NIST Chemical Kinetics Database, NIST Standard Reference Database 17, Version 7.0 (Web Version), Release 1.4.3, Data version 2008.12, NIST, <http://kinetics.nist.gov>